ACS Catalysis

Research Article

pubs.acs.org/acscatalysis

Mechanistic Insight into the Interaction Between a Titanium Dioxide Photocatalyst and Pd Cocatalyst for Improved Photocatalytic Performance

Ren Su,[†,‡] Nikolaos Dimitratos,[§,∥] Jinjia Liu,[‡,○] Emma Carter,[⊥] Sultan Althahban,[#] Xueqin Wang,[†] Yanbin Shen,[†,‡] Stefan Wendt,[†] Xiaodong Wen,[‡,○] J. W. (Hans) Niemantsverdriet,[‡,◆] Bo B. Iversen,[†,∇] Christopher J. Kiely,[#] Graham J. Hutchings,[*,§,∥] and Flemming Besenbacher[*,†]

[†]Interdisciplinary Nanoscience Centre (iNANO), Aarhus University, DK-8000 Aarhus C, Denmark

[‡]SynCat@Beijing, SynfuelsChina Co. Ltd., Leyuan South Street II, No.1, Yanqi Economic Development Zone C#, Huairou District, Beijing 101407, China

[§]Cardiff Catalysis Institute, School of Chemistry, Cardiff University, Cardiff CF10 3AT, United Kingdom

[∥]The UK Catalysis Hub, Research Complex at Harwell, Rutherford Appleton Laboratory, Oxfordshire, OX11 0FA, United Kingdom

[⊥]School of Chemistry, Cardiff University, Cardiff CF10 3AT, United Kingdom

[#]Department of Materials Science and Engineering, Lehigh University, 5 East Packer Avenue, 18015-3195 Bethlehem, Pennsylvania, United States

[∇]Department of Chemistry, Aarhus University, Langelandsgade 140, DK-8000 Aarhus C, Denmark

[○]State Key Laboratory of Coal Conversion, Institute of Coal Chemistry, CAS, Taiyuan, China

[◆]SynCat@DIFFER, Syngaschem BV, Eindhoven, The Netherlands

Supporting Information

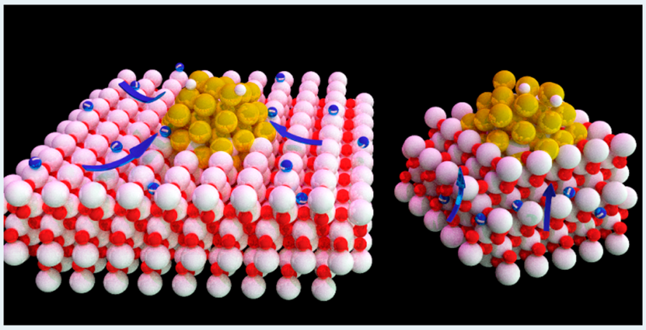

ABSTRACT: Understanding the cocatalyst/semiconductor interaction is of key importance for the design and synthesis of next generation photocatalytic materials for efficient hydrogen production and environmental cleanup applications. Here we investigate preformed Pd nanoparticles (NPs) supported on a series of anatase TiO_2 having well-controlled but varying degrees of crystallinity and crystallite size, and explore their photocatalytic performance for H_2 production and phenol decomposition. While tuning the anatase crystallite size significantly influences the photocatalytic performance, varying the TiO_2 crystallinity shows a negligible effect. Interestingly, the optimum quantum efficiency (~78%) for H_2 evolution is achieved with anatase having medium crystallite size (~16 nm), whereas for phenol decomposition, a promotional effect is only observed for anatase with larger crystallite sizes (>20 nm). Surface radical species and radical densities study reveal that the photogenerated charge carriers have been trapped at different sites depending on the crystallite size of anatase. While the excited electrons are only trapped in bulk lattice sites in small anatase (<16 nm), larger anatase particles provide extra surface sites for charge trapping, which benefit charge storage and transportation to Pd surface sites, leading to a more efficient utilization of charge carriers for photocatalysis. Additionally, Pd supported on medium sized anatase (~16 nm) hinders the formation of $O_2^{\bullet-}$ radicals on TiO_2 surfaces, thus preventing unwanted reoxidation of photogenerated H_2.

KEYWORDS: *photocatalysis, metal−semiconductor interaction, electron spin resonance, hydrogen evolution, phenol decomposition, TiO_2, density functional theory*

INTRODUCTION

Investigations of advanced catalytic processes have received significant attention, as the demand for sustainable energy, purified water, and clean air keeps increasing.[1−3]Photocatalysis employing particulate semiconductor based materials has experienced tremendous research activity due to the potential of using solar energy as the driving force for H_2 production, CO_2 reduction, and water and air remediation.[4−6] Numerous photocatalyst materials ranging from simple oxides,[7] nitrides,[8,9] or sulfides[10,11] to complicated mixed phase materials[12−14] have

Received: April 5, 2016
Revised: May 22, 2016
Published: May 24, 2016

DOI: 10.1021/acscatal.6b00982
ACS Catal. 2016, 6, 4239−4247

been developed for various applications; however, their photocatalytic performance still needs to be improved before implementation in industry can be anticipated.

The relatively poor performance of most photocatalyst materials can be directly linked to the kinetics of photoexcited electron−hole (e^-−h^+) pairs within the semiconductor, where most of them recombine rather than being separated and used for redox reactions with the surface adsorbed reactants.[15−17] Engineering the electronic properties of the photocatalyst by tuning the composition, structure, surface defects (impurities), surface acidity, and polymorph identity may improve the charge transfer dynamics as well as the optical properties of the material to optimize the photocatalytic performance.[18−22]

Decorating the surface of the photocatalyst by metal (i.e., Au, Pd, Pt) nanoparticles (NPs) is considered to be a promising and efficient approach to improve the photocatalytic performance.[23,24] The presence of metal NPs as a cocatalyst facilitates the spatial separation of the e^-−h^+ pairs by trapping the excited e^- that is transferred from the conduction band (CB) of the semiconductor photocatalysts.[25] Fundamental investigations of metal−semiconductor systems indicate that the elemental identity, size, and loading of the cocatalyst all influence the kinetics of the charge transfer process therefore affecting the photocatalytic performance.[26−29]

Meanwhile, it has been shown that the nature of the semiconductor support (i.e., polymorph composition, particle size) can also be used to manipulate the electronic properties of the metal NPs and thus lead to tunable photoreactivity and selectivity.[30,31] While promotional effects have been observed in most cases,[31−36] inhibition of the catalyst performance has been also noted.[37,38] This heterogeneity suggests that numerous details of the interplay between semiconductor photocatalyst particles and the cocatalyst NPs are still unclear. It has been well-established that well-controlled and deliberately engineered cocatalyst structures can have a significant positive influence the photoreactivity of the system.[39,40] However, the effect of modifying the semiconductor support to alter the semiconductor/cocatalyst interplay and thus engineering the overall photoreactivity remains largely unknown presumably because of the lack of a well-defined system with tunable physical parameters. Recently, the influence of crystallinity and crystallite size of the pristine anatase TiO_2 as the photocatalyst has been investigated, indicating that the reaction pathways of photocatalytic phenol decomposition can be tuned by adjusting the anatasenanocrystallite size.[41] Since varying the crystallinity and crystallite size can result in changes in the surface properties of anatase, we consider that these parameters may be deliberately controlled to modulate the interaction between metal NPs and semiconductor materials and thus enable fine-tuning of the overall photocatalytic performance of the system.

From the perspective of the reaction mechanism, most photocatalytic processes involve radical species (i.e., $OOH^\bullet$, $OH^\bullet$, O_2^-, and Ti^{3+}) that are created from the photogenerated e^-−h^+ pairs.[16] According to electron spin resonance spectrometry (ESR) analysis, the identity, concentration, and lifetime of radicals are crucial parameters that dictate the photoreactivity and selectivity of the catalyst.[30,42,43] Surface science studies on model systems have shown that fine-tuning of the cocatalyst/semiconductor interaction may alter the aforementioned parameters to allow some control over the reaction mechanism.[44,45] Unfortunately, such an investigation is still missing for well-defined systems of real photocatalysts, limiting our understanding of photocatalytic processes and hence the development of high performance photocatalysts.

Here we explore the cocatalyst/semiconductor interaction using preformed Pd NPs supported on well-defined nanoscale anatase TiO_2 particles. The Pd NPs prepared by sol-immobilization were deposited onto anatase synthesised using a supercritical methodology.[46] By producing the TiO_2 this way we can systematically and independently control the anatase crystallinity (12%−82%) and mean crystallite size (6−27 nm). The photocatalytic performance of this matrix of materials was investigated for photocatalytic H_2 evolution and phenol decomposition reactions to examine the interaction between the Pd cocatalyst and anatase support particles. In particular, we have probed the interaction mechanisms by following the identity and population density of surface radicals by ESR spectrometry. Additionally, we also employed theoretical calculations to rationalize the origins of the different radical species and to correlate the photocatalytic performance with the electronic properties of the materials.

RESULTS AND DISCUSSION

Physical Properties of the Photocatalysts. The XRD patterns of samples after immobilization of Pd NPs are shown in Figure 1. Diffraction patterns of Pd supported anatase samples with variable crystallinity (Figure 1a) and crystallite size (Figure 1b) remained almost identical compared to that of their pristine anatase equivalent (Figure S1),[41] indicating that the sol-immobilization process did not significantly alter the structure, mean crystallite size, or crystallinity of the anatase particles (Figure 1c). The diffraction peaks of Pd were not observed in all cases due to its ultrasmall size and low loadings (1 wt %). However, we do observe a very broad peak located at ∼32° (yellow zone in Figure 1a) within low crystallinity samples (i.e., 12.6%−60%), which can be tentatively assigned to PdO (101).[47]

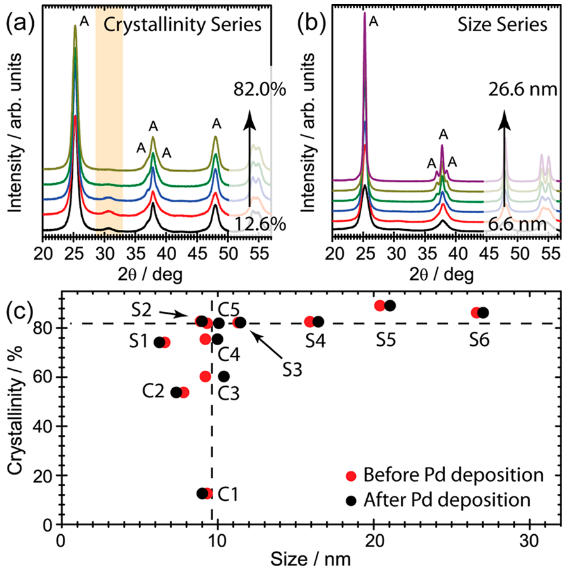

Figure 1. (a and b) XRD patterns of as-prepared Pd NPs on anatase TiO_2 particles having different crystallinity and mean crystallite size, respectively. "A" indicates the peak positions of anatase. (c) Comparison of the mean crystallite size of anatase before and after Pd immobilization as derived from Scherrer analysis of the XRD patterns. On the basis of comparisons of the XRD patterns, the crystallinity and mean crystallite size of anatase particles were considered to be unchanged after Pd addition.[41,48]

Meanwhile, PdO was not observed within the highly crystalline samples (Figure 1b), indicating the Pd^0 sol supported on a more disordered TiO_2 surface tends to become more oxidized at ambient conditions.

A subset of Pd/TiO_2 catalyst samples was examined in some detail using an aberration corrected STEM. A typical low magnification HAADF image from the Pd/TiO_2 (sample S6) photocatalyst is shown in Figure 2a. It is clear that the dispersion of Pd NPs on TiO_2 resulting from the sol-immobilization process is not particularly homogeneous, where some grains are more highly decorated with Pd cocatalyst NPs than others. Higher magnification HAADF images (Figure 2b) clearly show that the Pd NPs have a tendency to "wet" the TiO_2, forming an extended flat interface. In addition to the metallic Pd NPs, it was relatively easy to observe sub-nanometer Pd-containing clusters dispersed on anatase that were much smaller than the original colloid size.The formation of flattened interfaces and sub-nanometer clusters suggests that some PVA-ligand disruption and Pd diffusion has occurred during the drying process (120 °C for 16 h). Similar Pd cocatalyst morphologies and dispersions were found in other Pd/TiO_2 samples irrespective of the degree of crystallinity or the mean crystallite size of TiO_2 support (see Figures S1−S4 of samples C1, S2, S4, and S6 in the Supporting Information).[48] The particle size distributions of TiO_2 in the three 82% crystallinity samples (S2, S4, and S6) are plotted in Figure 2c and show very good agreement with the mean crystallite size analysis derived from the XRD measurements, indicating that sintering and agglomeration of the TiO_2 particles during Pd immobilization is negligible. Although there is some degree of overlap between samples S2, S4, and S6, it is fair to say that samples S2, S4, and S6 are mainly composed of small to medium (5−15 nm), medium (12−22 nm), and medium to large (17−30 nm) sized anatase particles, respectively. The corresponding Pd NP size distributions from these same samples are shown in Figure 2c and have mean values of the 2.3−3.1 nm range which is consistent with the starting size of the PVA stabilized Pd colloid.

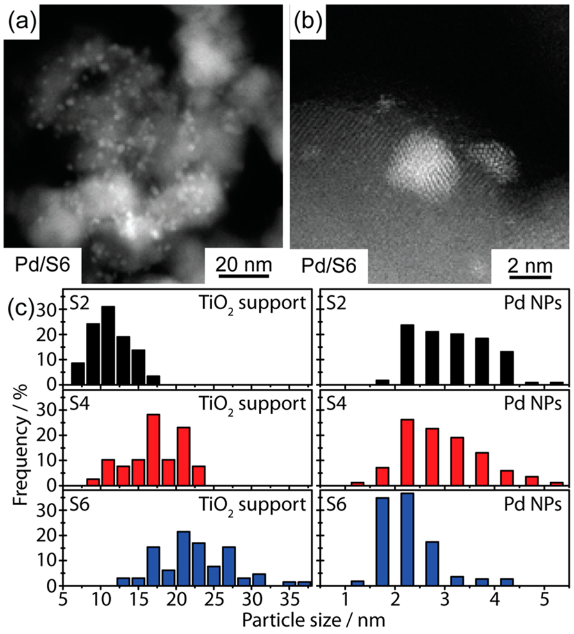

Figure 2. (a, b) Representative BF- and HAADF-STEM images of Pd on TiO_2 (sample S6). (c) Particle size distributions of the TiO_2 particles and Pd NPs of samples S2, S4, and S6.

We further characterized the surface composition and valence states of all as-synthesised Pd NPs dispersed on various anatase particles, as shown in the XPS spectra (Figure 3). Survey spectra of the photocatalysts as a function of the TiO_2 crystallinity (Figure 3a) and mean crystallite size (Figure 3b) revealed that within the limit of detectability they only consisted of Ti, O, Pd, and adventitious C. Quantitative analysis showed that the surface concentrations of Pd were ~2.5 wt % for all samples, which is slightly higher than the nominal 1 wt % bulk Pd concentration due to the preferential location of Pd at the anatase surface.

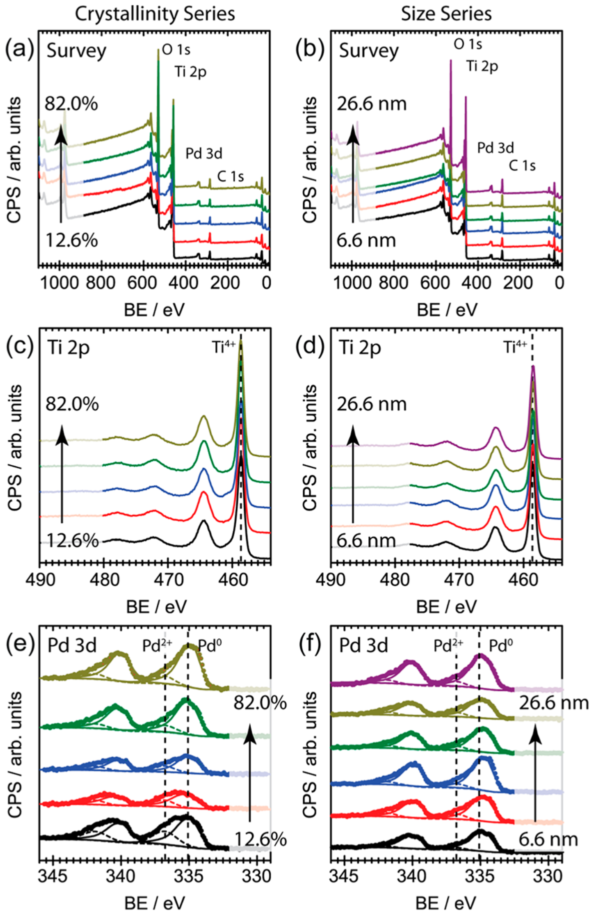

Figure 3. Survey XPS spectra of Pd NPs supported on (a) 9 nm anatase having different degrees of crystallinity and (b) 82% crystallinity with varying mean crystallite size, respectively. (c−f) High resolution Ti 2p and Pd 3d spectra of sample sets with varying TiO_2 crystallinity and varying mean crystallite size, respectively. The solid and dashed lines are fitting results of the raw data (dots). The binding energies of Ti^{4+}, Pd^0, and Pd^{2+} are indicated by dotted lines, respectively.[49,50] All catalysts have a nominal Pd loading of 1 wt %.

High resolution Ti 2p spectra of the crystallinity series (Figure 3c) and mean crystallite size series (Figure 3d) suggest that, as expected, exclusively Ti^{4+} is presented in all cases, again confirming that the anatase TiO_2 particles remained within the sol-immobilization process essentially unchanged. The Pd 3d spectra of all samples with different crystallinity and crystallite size are shown in Figure 3e,f, respectively. The Pd 3d signals can be deconvoluted at least into two peaks, indicating the presence of both Pd^0 and Pd^{2+} species.[50] However, the Pd^0/Pd^{2+} ratios varied significantly depending on the degree of crystallinity exhibited by the anatase TiO_2 particles. While the Pd^0/Pd^{2+} ratio increased from 2.4 to 6.7 following the increase of crystallinity from 12.6% to 82%, increasing the crystallite size of anatase showed negligible effect on the Pd^0/Pd^{2+} ratio, which remained at ~7 (see Table S2 in Supporting Information).[48] In conjunction with the evidence from the corresponding XRD patterns (Figure 1a), we can conclude that a mixture of Pd/PdO NPs has been deposited on anatase particles with low crystallinity, whereas for highly crystalline anatase, mainly metallic Pd NPs are formed that are possibly covered with an ultrathin PdO layer.

Effect of TiO_2 Structural Parameters on the Photocatalytic Performance. We first studied the effect of the Pd−anatase interaction on photocatalytic H_2 production, as shown in Figure 4. For comparative purposes, a sol-immobilized Pd cocatalyst supported on a commercial TiO_2 (Degussa P25) was also tested. Time resolved H_2 evolution (Figure 4a,b) suggests that all Pd/anatase variants can generate H_2 upon UV irradiation; however, the performance of these variants varied significantly depending on the nature of the anatase particles. To better visualize the effects of varying TiO_2 crystallinity and crystallite size, we calculated the H_2 production rate and apparent quantum efficiency (AQE) of all Pd/TiO_2photocatalysts, as shown in Figure 4c,d, respectively.[48] While poorly crystalline 9 nm TiO_2 particles (<60%) showed nearly identical performance for H_2 evolution, a slight increase in the performance was observed for those samples displaying a higher degree of crystallinity (>60%). Interestingly, increasing the crystallite size of the most crystalline TiO_2 particles (~82%) from 6.6 to 15.9 nm caused a significant enhancement in performance, but a further increase of the crystallite size to 26.6 nm deactivated the photoreactivity. Remarkably, the Pd NPs supported on the 15.9 nm, 82% crystalline anatase particles presented an extremely high AQE for H_2 evolution (~78%), which was about double that found for Pd NPs with similar particle size supported on commercial P25 TiO_2. Such an AQE value is even higher than that reported previously for the $Au_{core}Pd_{shell}$ cocatalyst on P25 (73%), which at the time of publication was superior to that of any photocatalyst reported using renewable organic chemicals as scavengers.[27]

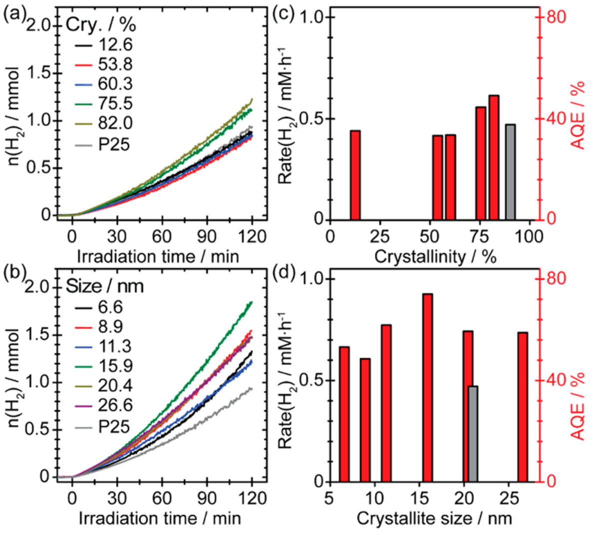

Figure 4. Time resolved photocatalytic H_2 evolution using 1 wt % Pd NPs supported on (a) 9 nm anatase with different crystallinity and (b) 82% crystallinity and varying crystallite size, respectively. A 1 wt % Pd NPs on Degussa P25 was tested for comparison. A 25 vol % of ethanol solution was used for all tests. (c, d) Derived H_2 production rates and AQE as a function of varying crystallinity and varying crystallite size of the anatase particles. AQE = $2n(H_2)/n(\text{incident photons})$, where $n(H_2)$ and $n(\text{incident photons})$ are the numbers of generated H_2 and incident photons, respectively.[48]

We further investigated the correlation of the Pd−anatase interaction and photocatalytic oxidation performance through a phenol decomposition reaction, as shown in Figure 5. Previous kinetic analysis based on *in situ* UV−vis and MS spectrometry suggested that the optimum performance for full phenol oxidation was always observed for samples that produced the minimum fraction of phenolic species (i.e., hydroquinone and benzoquinone), as these redox couples consume the photogenerated charge carriers continuously, thus reducing the conversion of phenol to CO_2.[39,41] Therefore, the decomposition rate of total phenolic species shown in Figure 5 reflects the performance of the photocatalysts for the full oxidation of phenol. For 9 nm TiO_2 with different degrees of crystallinity, surface decoration with Pd NPs showed negligible effects on the phenol decomposition rate for the more crystalline TiO_2 particles (>75%) but a decrease in phenol decomposition for the less crystalline TiO_2 (<60%) particles, respectively (Figure 5a). We did observe that the formation and decomposition of phenolic intermediates (hydroquinone and benzoquinone) were slightly improved upon increasing the crystallinity of the TiO_2 particles (Figure S8b,c),[46] which resulted in a minor enhancement toward the full decomposition of phenol using Pd/TiO_2 compared to that of their pristine TiO_2 counterparts.[41]

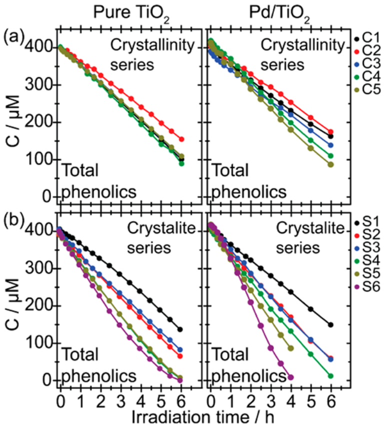

Figure 5. Evolution of total phenolics during photocatalytic phenol decomposition using the 9 nm pristine anatase (left column) and 1 wt % Pd NPs modified anatase (right column) with different crystallinity (a), and using the 82% pristine anatase (left column) and 1 wt % Pd NPs modified anatase (right column) with different mean crystallite size (b).[41]

Interestingly, Pd NPs supported on highly crystalline (82%) TiO_2 with tunable crystallite size presented a different phenomenon. While Pd NPs supported on small anatase particles (<15.9 nm) showed identical performance in phenol decomposition compared to their Pd-free counterparts, a further increase in the mean size of anatase (>15.9 nm) boosted the photocatalytic oxidation of phenol significantly (Figure 5b). The evolution of hydroquinone and benzoquinone using undecorated and Pd-decorated TiO_2 (82% crystallinity) with different mean crystallite sizes are also presented in Figure S8f,g, respectively.[41,46] These plots clearly reveal that the interaction of Pd with anatase can better promote the decomposition of both intermediates when the mean size of the anatase crystallites exceeds ~15.9 nm, which eventually accelerates the complete decomposition of phenol.

DOI: 10.1021/acscatal.6b00982
ACS Catal. 2016, 6, 4239−4247

We can satisfactorily explain some of the observed phenomena using some prior experience and knowledge. For example, amorphous TiO_2 is generally considered to be poor for photocatalysis.[41] Furthermore, the optimized photocatalytic H_2 production noted for medium sized crystalline anatase decorated with Pd can be considered as a deliberate trade-off between surface area effects and quantum size effects. However, the underlying mechanism is not sufficiently well-understood to fully explain the following issues: (i) the fact that increasing the degree of crystallinity of the anatase does not seem to significantly affect the photocatalytic H_2 production and phenol decomposition, and (ii) the optimized crystallite size required for photocatalytic H_2 production and phenol decomposition is markedly different (i.e., 15.9 nm versus 26.6 nm). Surface science studies on model TiO_2 photocatalysts revealed that surface defects (i.e., vacancies and adatoms) and bulk defects affect the charge transfer and trapping kinetics, which in turn control the surface adsorbed species that influence the reaction pathways and determine catalytic performance.[15,51] However, the above conclusions were drawn from data collected using the surface science approach based on single crystal TiO_2 (normally a reduced rutile phase) under ultrahigh vacuum conditions, which are not directly comparable to the TiO_2 NPs (normally pure anatase or mixed anatase/rutile polymorphs [P25]) that are used in real photocatalytic reactions under ambient conditions.

To rationalize the Pd–anatase interaction under different reaction conditions, we performed solid state ESR analysis on a selected subset of anatase samples and their corresponding Pd decorated counterparts, as shown in Figure 6. When pristine TiO_2 samples were irradiated under high vacuum (Figure 6a, $P_{cell} = 10^{-5}$ mbar), well-characterized Ti^{3+}centers, CB electrons (e^-_{CB}), and $O^{\bullet-}$ were formed as expected due to charge separation ($e^- + Ti^{4+} \rightarrow Ti^{3+}$, $O^{2-} + h^+ \rightarrow O^{\bullet-}$). Note that e^-_{CB} showed a g value of 2.003, which can effectively be considered as "free electrons" ($g = 2.0023$). The ESR signal at $g = 2.003$ could also be induced by the defect states at particle–particle interfaces on reduced anatase,[52] but such contribution should be negligible in our case as all samples consist of stoichiometric TiO_2. However, the relative concentrations of different radical species varied significantly as the crystallinity changed. While mainly Ti^{3+} species in regular bulk lattice positions (bulk Ti^{3+}, $g_\perp = 1.992$, $g_\parallel = 1.960$) were detected for TiO_2 with poor crystallinity or small sizes (C1, C3, C5, and S3),[53] Ti^{3+} in a disordered environment (near-surface Ti^{3+}, $g = 1.93$), e^-_{CB}, and $O^{\bullet-}$ were the dominant species found for highly crystalline TiO_2 with larger crystallite sizes (S4 and S6).[54] Because the most intense surface Ti^{3+} features were observed on sample S6, and the extensive bulk Ti^{3+} features were observed on samples C1, C3, C5, and S4, we surmise that large anatase is responsible for the surface Ti^{3+} and small anatase is the source for the bulk Ti^{3+}. Moreover, increasing the crystallinity from 12.6% (C1) to 60.3% (C3) and then to 82% (C5 and S3) solely resulted in an increase of the bulk Ti^{3+}, whereas most e^-_{CB} converted to near-surface Ti^{3+}centers when the TiO_2 size grew from 16.4 nm (S4) to 27 nm (S6). Therefore, the e^-_{CB} should be solely generated on medium sized anatase as the corresponding ESR peak was significantly observed on sample S4 and visible on sample S6. Interestingly, the signals of excess charges vanished almost completely in all samples when preformed Pd NPs were immobilized onto the TiO_2 particles (see Figure 6c), indicating most of the excited electrons were successfully transferred from TiO_2 and localized at Pd surface sites. In comparison, Ti^{3+} species in regular bulk lattice positions were predominantly detected for pure P25 after irradiation under high vacuum, which is a similar situation to that of sample S3 (Figure S10a). These trapped electrons can also be transferred to Pd surface sites (Figure S10c).[46]

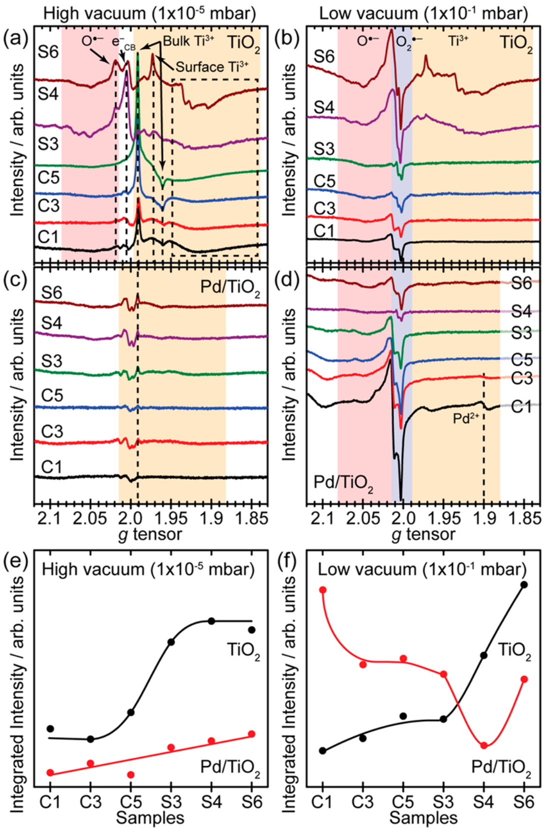

Figure 6. ESR spectra of selected pristine TiO_2 and 1 wt % Pd/TiO_2 samples that have been UV irradiated for 30 min at 77 K under high vacuum (a and c) and low vacuum (b and d), respectively. (e, f) Integrated intensities of all ESR spectra recorded under high vacuum and low vacuum, respectively. Lines in parts e and f are guidelines only.

We also performed similar experiments under low vacuum conditions ($P_{cell} = 10^{-1}$ mbar) to examine the effect of oxygen and water upon radical formation under UV irradiation, as shown in Figure 6b,d for pristine TiO_2 and Pd/TiO_2, respectively. Surprisingly, while surface Ti^{3+}, $O_2^{\bullet-}$, and $O^{\bullet-}$ were observed for large anatase particles (S4 and S6), $O_2^{\bullet-}$ was the only radical species detected for poorly crystalline or small grain TiO_2 samples (C1, C3, C5, and S3), and the intensity was much weaker compared to that observed for samples S4 and S6. The spectra changed considerably in the presence of Pd NPs on TiO_2 particles, as shown in Figure 6d. While the characteristic near-surface Ti^{3+} signals observed for large pristine anatase vanished due to charge transfer from TiO_2 to Pd, weak fingerprints of Pd^{2+} signals were observed in the low crystallinity sample (C1 and C3),[55] which agrees well with our XRD and XPS observations. Noticeably, the number of surface $O_2^{\bullet-}$ radicals decreased when increasing the crystallinity from 12.6% (C1) to 60.3% (C3) and to 82% (C5 and S3), as well as increasing the crystallite size from 9.3 nm (C5) to 11.3 nm (S3) and to 15.9 nm (S4), and reached a minimum with a mean size of 15.9 nm (S4). The concentration of $O_2^{\bullet-}$ radical shown in Figure 6d can also be associated with the divergence in the content of medium sized anatase between samples S3, S4, and S6. Surface Ti^{3+} and $O_2^{\bullet-}$ were the dominant species when pure P25 was irradiated under low vacuum, and the intensity of the $O_2^{\bullet-}$ signal was similar to that of S4 (Figure S10b). However, Ti^{3+} cations were still evident in the ESR spectra of Pd

DOI: 10.1021/acscatal.6b00982
ACS Catal. 2016, 6, 4239–4247

on P25, indicating the interfacial charge transfer between P25 and Pd to be relatively poor compared to that of the Pd-anatase system (Figure S10d).[46]

We have further estimated the total numbers of active paramagnetic species by integrating the ESR signals, as shown in Figure 6e,f. Under high vacuum conditions (Figure 6e), small TiO_2 particles with low crystallinity (C1, C3, and C5) generated far fewer active paramagnetic species compared to that of other TiO_2 particles. However, for large TiO_2 particles with high crystallinity (S3, S4, and S6), the number of Pd NPs seems to become insufficient for trapping excess Ti^{3+}. Under low vacuum conditions (Figure 6f), the densities of surface active paramagnetic species increased sharply only when the crystallinity and size of TiO_2 reached certain thresholds (>80% and >15.9 nm), and a minimum concentration of surface $O_2^{\bullet -}$ species was observed for Pd NPs supported on TiO_2 with a crystallite size of 15.9 nm (S4).

Since the density and identity of surface radicals are a reflection of the thermodynamics and kinetics of the charge carriers under reaction conditions, it is crucial to obtain a deep understanding of the charge carriers. In this connection we note that various defects such as OH species, low coordinated ions, and oxygen vacancies (V_O) may exist in pure TiO_2,[56−58] turning it into an n-type semiconductor, where the electrons and holes are the majority and minority charge carriers, respectively. However, in the present study all samples were stoichiometric anatase (see Figure 3) that should be close to behaving like intrinsic semiconductors. Nevertheless, excess charge may occur due to minority defects. In the following we focus on the excited electrons for H_2 evolution with ethanol as the hole scavenger. As the phenol decomposition is more complicated, we would have to consider both electrons and holes since phenol and O_2 have to be oxidized and reduced simultaneously.

In order to reveal the effect of charge carriers on the photocatalytic performance, we have modeled a three-layer anatase TiO_2 (101) surface with a V_O placed at various surface and subsurface (bulk) sites (Figure 7a), and calculated the surface DOS of the system with different V_O and the LUMO distributions, as shown in Figure 7. Our focus here is the creation of Ti^{3+} in the system rather than the structure of the defects. Here, introducing one V_O corresponds to the creation of two Ti^{3+}, which is equivalent to two trapped electrons at the Ti^{4+} sites.

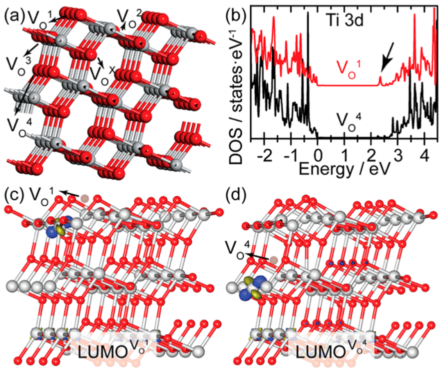

Figure 7. (a) Three-layer anatase (101) surface model with five different oxygen vacancies (V_O). (b) The surface DOS of Ti 3d with V_O^1 and V_O^4. The arrow indicates the midgap state. (c, d) LUMO of the anatase (101) surface with V_O^1 and V_O^4, respectively. Ti atom: gray. O atom: red.

Among these five possible V_O sites shown in Figure 7a, V_O^1, V_O^2, V_O^3, and V_O^X can be assigned to different variants of surface V_O, whereas V_O^4 is a subsurface V_O defect. The calculated formation energies derived from the model with one single V_O^1, V_O^2, V_O^3, V_O^X, and V_O^4 defect are 3.99, 4.90, 4.57, 4.27, and 3.88 eV at 0 K, respectively (see Figure S11),[46] indicating that oxygen vacancies are most stable on site 4 (i.e., subsurface) followed by site 1 (surface) rather than on the other sites considered.

The surface DOS shown in Figure 7b reveals the effect of V_O^1 and V_O^4 on the Ti 3d orbitals, which constitute the conduction band of TiO_2. Interestingly, a midgap state close to the unoccupied Ti 3d orbitals was observed for anatase with a V_O^1 type defect (see arrow), whereas such a feature was not found for anatase with a V_O^4 defect. This Ti 3d midgap level induced by the surface V_O provides additional trapping sites for the excited electrons, which could be transferred to the Pd NPs for use in subsequent reduction reactions. Meanwhile, the location of V_O has a negligible effect on the O 2p orbitals in the valence band (Figure S12);[46] thus, the exact location of V_O does not influence the hole species significantly. The relatively high intensity ESR signals of $O^{\bullet -}$ observed in samples S4 and S6 in Figure 6a are probably due to the enhanced charge separation caused by the midgap states that originate from surface defects. We further mapped the LUMO of the anatase (101) surface with V_O^1 and V_O^4, as shown in Figure 7c,d. Obviously the LUMO located at the surface Ti sites (adjacent to the V_O^1 site) is more feasible for charge trapping and subsequent charge transfer than the LUMO located at the subsurface Ti sites (adjacent to the V_O^4 site). Previous surface science studies and DFT calculations showed that the subsurface and bulk V_O's are significantly more stable on highly reduced anatase (101).[57] However, in our case, the samples are all very close to stoichiometric TiO_2 (see Figure 3); TiO_2 particles are used instead of single crystals, and we are also not working under ultrahigh vacuum conditions. Hence, other surface defects can also potentially be envisaged to be present on our samples that lead to Ti^{3+} excess charge.[57] Although all calculation results were derived at 0 K, the electrons that have been trapped at the surface sites should be thermodynamically much easier to utilize for charge transfer even at room temperature. Moreover, the additional unoccupied Ti 3d states observed for the model with V_O^1 should be temperature independent.

We can now correlate the photocatalytic performance with the charge carriers and the properties of the photocatalyst materials by combining the ESR results with the insight of the theoretical calculations. For the H_2 evolution reaction, "free electrons" (e^-_{CB}) and surface trapped electrons (near-surface Ti^{3+}) are thermodynamically and kinetically more favorable to reduce H^+ to H_2 compared to electrons trapped within the subsurface or in the bulk (i.e., lattice Ti^{3+}). Ti^{3+} excess charge is available at the surface of large anatase crystals having high crystallinity, resulting in the formation of surface midgap states below the conduction band, thus improving the charge trapping and transfer efficiency. For anatase with low crystallinity and small crystallite size, Ti^{3+} excess charge is available predominantly in the subsurface or bulk, which results in a relatively poor charge trapping efficiency. Moreover, the unoccupied states are located at the subsurface or bulk that are unfavorable for interfacial charge transfer, leading to a relatively poor photocatalytic performance. Furthermore, a lower density of surface $O_2^{\bullet -}$ radicals in medium sized anatase is ideal to inhibit reoxidation (i.e., back reactions) of the freshly synthesized H_2 during the photocatalytic process.[40] Accordingly, an optimum level of photocatalytic H_2 evolution was observed for highly crystalline TiO_2 (82.6%) with moderate crystallite size (15.9 nm). The relatively poor performance of Pd on P25 can mainly be associated with the bulk trapped electrons that require extra energy for charge transfer to the Pd NPs. For phenol decomposition, however, a situation is favorable where a dense population of surface radicals exist, which makes breaking of the aromatic rings more feasible. Thus, the best performance for phenol decomposition was observed for highly crystalline TiO_2 (86.3%) of large size (26.6 nm).

■ CONCLUSIONS

We have synthesised photocatalysts composed of Pd NPs supported on TiO_2 (anatase) materials having well-controlled crystallinity and crystallite size. While mainly metallic Pd NPs were deposited on highly crystalline TiO_2 regardless of the anatase crystallite size, about 20−30% of the Pd was presented in the Pd^{2+} form (i.e., PdO) when using poorly crystalline TiO_2 particles. We have investigated the interaction of the Pd cocatalyst with TiO_2 for photocatalytic H_2 production and phenol decomposition reactions. Tuning the crystallinity of the TiO_2 particles showed a negligible effect on the photocatalytic performance of both reactions in comparison to varying the crystallite size. For H_2 production, a remarkable apparent quantum efficiency of ∼78% was obtained when using anatase particles with a medium crystallite size of ∼16 nm. Meanwhile, an improvement in phenol decomposition was only observed for anatase particles with larger crystallite size (>20 nm). ESR analysis revealed that larger anatase particles (>16 nm) offer more near-surface sites for charge trapping, whereas solely bulk trapping sites were observed for smaller anatase. Such additional surface sites benefit both charge storage and charge transfer from TiO_2 to the Pd cocatalyst surface sites, and thus provide a more efficient utilization of charge carriers to enhance H_2 evolution and phenol decomposition. Additionally, the presence of Pd on medium sized anatase particles (∼16%) limited the formation of $O_2^{\bullet -}$ radicals on TiO_2 surfaces, preventing unwanted reoxidation of photogenerated H_2. DFT calculations on surface DOS and LUMO distribution illustrate that the surface trapping sites for photoexcited electrons in medium and large grain anatase can indeed be associated with different locations of defects such as V_O species. Irrespective of the exact nature of the defects, it is clear that surface Ti^{3+} sites are beneficial for photocatalytic reactions, since they facilitate interfacial charge transfer from TiO_2 to the Pd NPs. Our results suggest that varying the size of the semiconductor is an efficient method to tune the electronic interaction between metal NPs and semiconductor to improve the photocatalytic performance. Further investigation on the Pd size effect, Pd^0:Pd^{2+}ratio, and Pd/TiO_2 interface may further tune the electronic properties of the material thus improving the photocatalytic performance.

■ EXPERIMENTAL SECTION

Sample Preparation. *Synthesis of TiO_2 Particles.* A supercritical synthesis approach using a continuous flow reactor was employed to prepare TiO_2 nanoparticles.[46] Isopropanol mixed with deionized (DI) water and titanium isopropoxide (TTIP, ACROS, 98%) were used as the supercritical solvent and the reactant, respectively. The crystallinity and crystallite size of pure anatase TiO_2 were controlled by tuning the concentration of TTIP, composition of the solvent, flow rate, temperature, and pressure, as listed in Table S1 in the Supporting Information.[48] The suspensions of as-prepared anatase particles were centrifuged, washed with DI water, and dried overnight at 120 °C. A series of samples were prepared where the crystallinity of anatase was tuned independently from 12% to 82% while maintaining a constant crystallite size of ∼9 nm (samples C1−C5). A second series was made where the anatase crystallite size was varied from ∼6 to ∼27 nm while keeping a constant crystallinity of ∼82% (samples S1−S6), as shown in Figure S1.[41,48]

Deposition of Pd NPs on TiO_2 Particles. A standard sol-immobilization method was utilized to deposit 1 wt % of Pd NPs on the various anatase particles described above.[32] Aqueous solutions of $PdCl_2$ (Johnson Matthey), polyvinyl alcohol (PVA) (1 wt % aqueous solution, Aldrich, MW = 10 000, 80% hydrolyzed), and $NaBH_4$ (0.1 M) were freshly prepared and mixed to generate the Pd colloid for deposition. Immobilization of the Pd colloid was then performed by adding the anatase support into the fresh sol (acidified to pH 1−2 by sulfuric acid) under vigorous stirring conditions. The catalyst slurry was then filtered, washed thoroughly with DI water, and dried at 120 °C overnight. For comparative purposes, a 1 wt % Pd supported on commercial TiO_2 (Degussa P25) was also prepared by sol-immobilization.

Materials Characterization. Powder X-ray diffraction (XRD) was used to acquire crystallographic information on the samples by using an X-ray diffractometer (SmartLab, Rigaku) operating with Cu Kα radiation. A scan rate of 0.04 deg s^{-1} and integration time of 10.0 s were used for all measurements. Rietveld refinement was applied to determine the peak area and thus the crystallite size from the diffraction patterns.[41,59] The crystallinity of the sample is defined as the percentage of crystallites in a mixture of crystalline and amorphous material, and thus can be measured by mixing the sample with a CaF_2 reference (1:1 weight ratio), which is 100% crystalline. The crystallinity of the sample was calculated by comparing the integrated areas of the diffraction peaks of anatase (101) with CaF_2 (111) by the following equation:[60]

$$\text{crystallinity} = 0.763 \times A_{\text{anatase}(101)}/A_{\text{CaF}_2(111)} \times 100\% \quad (1)$$

High angle annular dark-field (HAADF) images of some of the photocatalyst samples were acquired using a 200 kV JEOL ARM 200CF scanning transmission electron microscope (STEM) equipped with a CEOS probe aberration corrector. The samples for STEM analysis were prepared by dry dispersing the catalyst powder onto a holey carbon TEM grid.

A Kratos Axis Ultra spectrometer equipped with a monochromatic Al Kα source (10 mA, 15 kV) was employed to perform X-ray photoelectron spectroscopy (XPS) analysis. Pass energies of 160 and 40 eV were used for survey scans and high resolution scans, respectively. Calibration of the binding energy was referenced to adventitious carbon, which has a binding energy of 284.8 for the C 1s peak.

Photocatalytic Performance Measurements. Photocatalytic H_2 production and phenol decomposition reactions were both performed to evaluate the performance of each material. Prior to the experiment, fresh photocatalyst (50 mg) was dispersed in DI water and subsequently cleaned by UV irradiation (Optimax 365, 365 nm LED, photon flux: 4×10^{17} photons s^{-1}) for 2 h to remove the PVA ligand.

For H_2 production, 6.25 mL of ethanol (99 vol %) was added to the reactor to form a 25 vol % ethanol−catalyst−water suspension (25 mL), which was transferred to a leak-tight reactor that was connected to a quadruple mass spectrometer (QMS, Hiden HPR-20) for the analysis of evolved H_2. The reactor was then evacuated using a bypass pump until the dissolved O_2 level was reduced to below 5 μM. UV irradiation of 2 h duration was then employed to photocatalytically evolve H_2 under conditions of continuous stirring at room temperature using the same LED light source as described above. The partial pressures of $m/e^- = 2$ (H_2), 18 (H_2O), 28 (N_2), 32 (O_2), and 44 (CO_2) species were monitored *in situ*.

For phenol decomposition, 1 mL of phenol solution (20 mM) was added to the reactor to form a 400 μM phenol−catalyst−water suspension (50 mL). An adsorption/desorption equilibrium was achieved by keeping the suspension in the dark for 1 h. Then, UV irradiation was commenced using the aforementioned LED light source to initiate the photocatalytic decomposition of phenol. A 1.5 mL aliquot of the suspension was collected at given time intervals, centrifuged, and analyzed by UV−vis spectrometry (UV-1800, Shimadzu, JP).

Further details of the photoreactivity measurements and related calculations are summarized in the Supporting Information and can also be found elsewhere.[28,39,48]

ESR Characterization of the Photocatalysts. An X-band Bruker EMX spectrometer equipped with a highly sensitive cavity (ER 4119HS) was utilized to record the ESR spectra of pure anatase and the various Pd/anatase samples that have been treated under different oxygen partial pressures. This has been realized by evacuating the cell using a turbo pump system (P_{cell}: 1×10^{-5} mbar) or a rotary pump (P_{cell}: 1×10^{-1} mbar), respectively. Before evacuation, the samples (10 mg) were cleaned by UV irradiation for 2 h at room temperature. The samples were then evacuated under dynamic vacuum at 80 °C (for low vacuum) and 120 °C (for high vacuum) to remove excess surface adsorbed water. The evacuated cell was then irradiated using the same UV light for 30 min at 77 K, and then transferred into the cavity which was held at 120 K to record ESR spectra. The modulation field and microwave power employed were 100 kHz and 10 mW, respectively. The value of the g tensor for each measurement was determined using a 2,2-diphenyl-1-picrylhydrazyl (DPPH) standard.[43,61]

Theoretical Calculations. Density functional theory (DFT) was used to calculate the formation energy of the photoexcited electrons that are trapped at surface and subsurface sites by creating surface and subsurface oxygen vacancies (V_O). Subsequently, the impact of various surface and subsurface V_O defects on the surface density of states (DOS) and the distribution of the lowest unoccupied molecular orbitals (LUMO) were also evaluated. A three O−Ti−O layer anatase model (144 atoms) was used to simulate the (101) surface (surface area 10.44×15.57 Å^2). Vienna Ab-Initio Simulation Package (VASP) with the frozen-core projected-augmented wave (PAW) method was used with application of the generalized gradient approximation (GGA) of Perdew−Burke−Ernzerhof (PBE).[62−65] The Ti 3d states were described by GGA + U with a U value of 3.5 eV to correct for the on-site Coulomb interactions.[66,67] The energy and the electronic properties of the anatase (101) surface were computed using a plane wave cutoff of 500 eV and a Monkhorst−Pack grid of ($2 \times 2 \times 1$) k-points.[68] The computational resources for the project were supplied by the Tianhe-2 in Lvliang, Shanxi province. More details of the calculation parameters can be found in the Supporting Information.[46]

ASSOCIATED CONTENT

Ⓢ Supporting Information

The Supporting Information is available free of charge on the ACS Publications website at DOI: 10.1021/acscatal.6b00982.

> Sample preparation and characterization, apparent quantum efficiency, evolution of the phenolic intermediates, additional ESR spectra, and additional calculation details (PDF)

AUTHOR INFORMATION

Corresponding Authors

*E-mail: hutch@cardiff.ac.uk.
*E-mail: fbe@inano.au.dk.

Notes

The authors declare no competing financial interest.

ACKNOWLEDGMENTS

We acknowledge the financial support from the iNANO Centre through the Danish Strategic Research Council and the Carlsberg Foundation, and the Centre for Materials Crystallography (Denmark National Research Foundation, DNRF93). We also acknowledge the EPSRC (EP/K014854/1) and NSFC (project number 21503257) for financial support. R.S. acknowledges financial support from Syngaschem BV and SynfuelsChina Technology Co. Ltd. for his stay at Cardiff University in 2014. R.S. would like to thank Prof. Damien Murphy at Cardiff University for EPR training and fruitful discussions and Dr. Jose Gracia at SynCat@Beijing for discussions in calculations.

REFERENCES

(1) Jin, F. M.; Zeng, X.; Liu, J. K.; Jin, Y. J.; Wang, L. Y.; Zhong, H.; Yao, G. D.; Huo, Z. B. *Sci. Rep.* **2014**, *4*, 4503−4511.

(2) Tedsree, K.; Li, T.; Jones, S.; Chan, C. W. A.; Yu, K. M. K.; Bagot, P. A. J.; Marquis, E. A.; Smith, G. D. W.; Tsang, S. C. E. *Nat. Nanotechnol.* **2011**, *6*, 302−307.

(3) Wong, M. S.; Alvarez, P. J. J.; Fang, Y.-l.; Akçin, N.; Nutt, M. O.; Miller, J. T.; Heck, K. N. *J. Chem. Technol. Biotechnol.* **2009**, *84*, 158−166.

(4) Liu, J.; Liu, Y.; Liu, N.; Han, Y.; Zhang, X.; Huang, H.; Lifshitz, Y.; Lee, S.-T.; Zhong, J.; Kang, Z. *Science* **2015**, *347*, 970−974.

(5) Sastre, F.; Puga, A. V.; Liu, L.; Corma, A.; García, H. *J. Am. Chem. Soc.* **2014**, *136*, 6798−6801.

(6) Chong, M. N.; Jin, B.; Chow, C. W. K.; Saint, C. *Water Res.* **2010**, *44*, 2997−3027.

(7) Li, R.; Weng, Y.; Zhou, X.; Wang, X.; Mi, Y.; Chong, R.; Han, H.; Li, C. *Energy Environ. Sci.* **2015**, *8*, 2377−2382.

(8) Wang, X.; Maeda, K.; Thomas, A.; Takanabe, K.; Xin, G.; Carlsson, J. M.; Domen, K.; Antonietti, M. *Nat. Mater.* **2009**, *8*, 76−80.

(9) Wang, L.; Dionigi, F.; Nguyen, N. T.; Kirchgeorg, R.; Gliech, M.; Grigorescu, S.; Strasser, P.; Schmuki, P. *Chem. Mater.* **2015**, *27*, 2360−2366.

(10) Zhang, Y. C.; Du, Z. N.; Li, K. W.; Zhang, M.; Dionysiou, D. D. *ACS Appl. Mater. Interfaces* **2011**, *3*, 1528−1537.

(11) Bao, N.; Shen, L.; Takata, T.; Domen, K. *Chem. Mater.* **2008**, *20*, 110−117.

(12) Moniz, S. J. A.; Shevlin, S. A.; Martin, D. J.; Guo, Z.-X.; Tang, J. *Energy Environ. Sci.* **2015**, *8*, 731−759.

(13) Nasalevich, M. A.; Becker, R.; Ramos-Fernandez, E. V.; Castellanos, S.; Veber, S. L.; Fedin, M. V.; Kapteijn, F.; Reek, J. N. H.; van der Vlugt, J. I.; Gascon, J. *Energy Environ. Sci.* **2015**, *8*, 364−375.

(14) García-López, E.; Marcì, G.; Megna, B.; Parisi, F.; Armelao, L.; Trovarelli, A.; Boaro, M.; Palmisano, L. *J. Catal.* **2015**, *321*, 13−22.

(15) Henderson, M. A. *Surf. Sci. Rep.* **2011**, *66*, 185−297.

(16) Hoffmann, M. R.; Martin, S. T.; Choi, W. Y.; Bahnemann, D. W. *Chem. Rev.* **1995**, *95*, 69−96.

(17) Tachikawa, T.; Fujitsuka, M.; Majima, T. *J. Phys. Chem. C* **2007**, *111*, 5259−5275.

(18) Su, R.; Christensen, M.; Shen, Y. B.; Kibsgaard, J.; Elgh, B.; Vang, R. T.; Bechstein, R.; Wendt, S.; Palmqvist, A.; Iversen, B. B.; Besenbacher, F. *J. Phys. Chem. C* **2013**, *117*, 27039−27046.

(19) Hernandez-Alonso, M. D.; Fresno, F.; Suarez, S.; Coronado, J. M. *Energy Environ. Sci.* **2009**, *2*, 1231−1257.

(20) Martin, D. J.; Qiu, K.; Shevlin, S. A.; Handoko, A. D.; Chen, X.; Guo, Z.; Tang, J. *Angew. Chem., Int. Ed.* **2014**, *53*, 9240−9245.

(21) Scanlon, D. O.; Dunnill, C. W.; Buckeridge, J.; Shevlin, S. A.; Logsdail, A. J.; Woodley, S. M.; Catlow, C. R. A.; Powell, M. J.; Palgrave, R. G.; Parkin, I. P.; Watson, G. W.; Keal, T. W.; Sherwood, P.; Walsh, A.; Sokol, A. A. *Nat. Mater.* **2013**, *12*, 798−801.

(22) Kozlov, D. V.; Vorontsov, A. V. *J. Catal.* **2008**, *258*, 87−94.

(23) Yang, J.; Wang, D.; Han, H.; Li, C. *Acc. Chem. Res.* **2013**, *46*, 1900−1909.

(24) Rawalekar, S.; Mokari, T. *Adv. Energy. Mater.* **2013**, *3*, 12−27.

(25) Takai, A.; Kamat, P. V. *ACS Nano* **2011**, *5*, 7369−7376.

(26) Subramanian, V.; Wolf, E. E.; Kamat, P. V. *J. Am. Chem. Soc.* **2004**, *126*, 4943−4950.

(27) Cozzoli, P. D.; Curri, M. L.; Agostiano, A. *Chem. Commun.* **2005**, *25*, 3186−3188.

(28) Su, R.; Tiruvalam, R.; Logsdail, A. J.; He, Q.; Downing, C. A.; Jensen, M. T.; Dimitratos, N.; Kesavan, L.; Wells, P. P.; Bechstein, R.; Jensen, H. H.; Wendt, S.; Catlow, C. R. A.; Kiely, C. J.; Hutchings, G. J.; Besenbacher, F. *ACS Nano* **2014**, *8*, 3490−3497.

(29) Priebe, J. B.; Radnik, J.; Lennox, A. J. J.; Pohl, M.-M.; Karnahl, M.; Hollmann, D.; Grabow, K.; Bentrup, U.; Junge, H.; Beller, M.; Brückner, A. *ACS Catal.* **2015**, *5*, 2137−2148.

(30) Tsukamoto, D.; Shiraishi, Y.; Sugano, Y.; Ichikawa, S.; Tanaka, S.; Hirai, T. *J. Am. Chem. Soc.* **2012**, *134*, 6309−6315.

(31) Murdoch, M.; Waterhouse, G. I. N.; Nadeem, M. A.; Metson, J. B.; Keane, M. A.; Howe, R. F.; Llorca, J.; Idriss, H. *Nat. Chem.* **2011**, *3*, 489−492.

(32) Su, R.; Forde, M. M.; He, Q.; Shen, Y.; Wang, X.; Dimitratos, N.; Wendt, S.; Huang, Y.; Iversen, B. B.; Kiely, C. J.; Besenbacher, F.; Hutchings, G. J. *Dalton Trans.* **2014**, *43*, 14976−14982.

(33) Paramasivam, I.; Macak, J. M.; Schmuki, P. *Electrochem. Commun.* **2008**, *10*, 71−75.

(34) Chen, X. B.; Liu, L.; Yu, P. Y.; Mao, S. S. *Science* **2011**, *331*, 746−750.

(35) Maeda, K.; Teramura, K.; Lu, D. L.; Saito, N.; Inoue, Y.; Domen, K. *Angew. Chem., Int. Ed.* **2006**, *45*, 7806−7809.

(36) Mizukoshi, Y.; Sato, K.; Konno, T. J.; Masahashi, N. *Appl. Catal., B* **2010**, *94*, 248−253.

(37) Primo, A.; Corma, A.; Garcia, H. *Phys. Chem. Chem. Phys.* **2011**, *13*, 886−910.

(38) Mogyorósi, K.; Kmetykó, Á.; Czirbus, N.; Veréb, G.; Sipos, P.; Dombi, A. *React. Kinet. Catal. Lett.* **2009**, *98*, 215−225.

(39) Su, R.; Tiruvalam, R.; He, Q.; Dimitratos, N.; Kesavan, L.; Hammond, C.; Lopez-Sanchez, J. A.; Bechstein, R.; Kiely, C. J.; Hutchings, G. J.; Besenbacher, F. *ACS Nano* **2012**, *6*, 6284−6292.

(40) Li, Y. H.; Xing, J.; Chen, Z. J.; Li, Z.; Tian, F.; Zheng, L. R.; Wang, H. F.; Hu, P.; Zhao, H. J.; Yang, H. G. *Nat. Commun.* **2013**, *4*, 2500−2507.

(41) Wang, X. Q.; Sø, L.; Su, R.; Wendt, S.; Hald, P.; Mamakhel, A.; Yang, C. X.; Huang, Y. D.; Iversen, B. B.; Besenbacher, F. *J. Catal.* **2014**, *310*, 100−108.

(42) Hurum, D. C.; Agrios, A. G.; Gray, K. A.; Rajh, T.; Thurnauer, M. C. *J. Phys. Chem. B* **2003**, *107*, 4545−4549.

(43) Carter, E.; Carley, A. F.; Murphy, D. M. *J. Phys. Chem. C* **2007**, *111*, 10630−10638.

(44) Matthey, D.; Wang, J. G.; Wendt, S.; Matthiesen, J.; Schaub, R.; Lægsgaard, E.; Hammer, B.; Besenbacher, F. *Science* **2007**, *315*, 1692−1696.

(45) Porsgaard, S.; Jiang, P.; Borondics, F.; Wendt, S.; Liu, Z.; Bluhm, H.; Besenbacher, F.; Salmeron, M. *Angew. Chem., Int. Ed.* **2011**, *50*, 2266−2269.

(46) Hald, P.; Becker, J.; Bremholm, M.; Pedersen, J. S.; Chevallier, J.; Iversen, S. B.; Iversen, B. B. *J. Solid State Chem.* **2006**, *179*, 2674−2680.

(47) Ganji, S.; Bukya, P.; Vakati, V.; Rao, K. S. R.; Burri, D. R. *Catal. Sci. Technol.* **2013**, *3*, 409−414.

(48) Details for sample synthesis and photocatalytic tests, additional TEM and XPS characterizations, and theoretical calculations can be found in Supporting Information.

(49) Su, R.; Bechstein, R.; So, L.; Vang, R. T.; Sillassen, M.; Esbjornsson, B.; Palmqvist, A.; Besenbacher, F. *J. Phys. Chem. C* **2011**, *115*, 24287−24292.

(50) Noack, K.; Zbinden, H.; Schlögl, R. *Catal. Lett.* **1990**, *4*, 145−155.

(51) Henderson, M. A.; Lyubinetsky, I. *Chem. Rev.* **2013**, *113*, 4428−4455.

(52) Baumann, S. O.; Elser, M. J.; Auer, M.; Bernardi, J.; Hüsing, N.; Diwald, O. *Langmuir* **2011**, *27*, 1946−1953.

(53) Chiesa, M.; Paganini, M. C.; Livraghi, S.; Giamello, E. *Phys. Chem. Chem. Phys.* **2013**, *15*, 9435−9447.

(54) Barolo, G.; Livraghi, S.; Chiesa, M.; Paganini, M. C.; Giamello, E. *J. Phys. Chem. C* **2012**, *116*, 20887−20894.

(55) Vedyagin, A. A.; Volodin, A. M.; Stoyanovskii, V. O.; Mishakov, I. V.; Medvedev, D. A.; Noskov, A. S. *Appl. Catal., B* **2011**, *103*, 397−403.

(56) Mi, J.-L.; Jensen, K. M. O.; Tyrsted, C.; Bremholm, M.; Iversen, B. B. *CrystEngComm* **2015**, *17*, 6868−6877.

(57) He, Y.; Dulub, O.; Cheng, H.; Selloni, A.; Diebold, U. *Phys. Rev. Lett.* **2009**, *102*, 106105.

(58) Di Valentin, C.; Pacchioni, G.; Selloni, A. *J. Phys. Chem. C* **2009**, *113*, 20543−20552.

(59) Rietveld, H. *J. Appl. Crystallogr.* **1969**, *2*, 65−71.

(60) Jensen, H.; Joensen, K.; Jørgensen, J.-E.; Pedersen, J.; Søgaard, G. *J. Nanopart. Res.* **2004**, *6*, 519−526.

(61) Adamski, A.; Spałek, T.; Sojka, Z. *Res. Chem. Intermed.* **2003**, *29*, 793−804.

(62) Kresse, G.; Joubert, D. *Phys. Rev. B: Condens. Matter Mater. Phys.* **1999**, *59*, 1758−1775.

(63) Kresse, G.; Furthmüller, J. *Phys. Rev. B: Condens. Matter Mater. Phys.* **1996**, *54*, 11169−11186.

(64) Kresse, G.; Hafner, J. *Phys. Rev. B: Condens. Matter Mater. Phys.* **1994**, *49*, 14251−14269.

(65) Perdew, J. P.; Burke, K.; Ernzerhof, M. *Phys. Rev. Lett.* **1996**, *77*, 3865−3868.

(66) Dudarev, S. L.; Botton, G. A.; Savrasov, S. Y.; Humphreys, C. J.; Sutton, A. P. *Phys. Rev. B: Condens. Matter Mater. Phys.* **1998**, *57*, 1505−1509.

(67) Cheng, H.; Selloni, A. *J. Chem. Phys.* **2009**, *131*, 054703.

(68) Blöchl, P. E. *Phys. Rev. B: Condens. Matter Mater. Phys.* **1994**, *50*, 17953−17979.